Vacuum 233 (2025) 113954

Contents lists available at ScienceDirect

Vacuum

journal homepage: www.elsevier.com/locate/vacuum

Characterization of 2D-PEA_2SnI_4 perovskite thin films grown by sequential physical vapor deposition

Alex Sembito [a,b], Margdaline Musanga Ligavo [a,b], Julius M. Mwabora [a], Francis W. Nyongesa [a], Mmantsae Diale [b,*]

[a] University of Nairobi, P.O. Box 30197-00100, Nairobi, Kenya
[b] University of Pretoria, Private Bag X20, Hatfield, 0028, South Africa

ARTICLE INFO

Handling Editor: Prof. L.G. Hultman

Keywords:
Sequential physical vapor deposition
Substrate temperature

ABSTRACT

2D-PEA_2SnI_4 perovskite thin films were prepared by sequential physical vapor deposition (SPVD) technique. The effect of low substrate deposition temperature, annealing time, and PEAI thickness on structural, optical, and morphological properties of 2D-PEA_2SnI_4 thin films was investigated. The results show that early-stage crystallization of SnI_2 films before subsequent evaporation of PEAI hinders the efficient interdiffusion of the perovskite precursors. Films deposited at low substrate temperature (~18 °C) exhibited ~300 % carrier lifetime improvement from 0.14 to 0.56 ns, suggesting a reduction of defect density and suppression of nonradiative recombination. FE-SEM micrographs revealed uniformly deposited films with densely packed grain size ranging from 92.50 to 453.1 nm and minimum pinholes. AFM results showed that surface roughness decreased from 138.2 to 50.99 nm as annealing time increased from 0 to 60 min. Similarly, surface roughness increased from 18.02 to 50.99 nm as PEAI thickness increased from 40 to 500 nm. XRD results revealed an improvement in crystallinity and average crystallite size as annealing time and PEAI thickness increased. This work suggests a way of improving the reaction between 2D-Sn-based perovskite precursors using the SPVD technique by controlling the substrate temperature and highlighting the role of substrate deposition temperature, film thickness, and annealing time towards crystallization of the perovskite.

1. Introduction

Perovskite materials have been dominated by three-dimensional (3D) organic-inorganic halide perovskites (OIHP), due to their suitability for applications in solar cells, photodetectors, light-emitting diodes (LEDs), etc [1,2]. These materials exhibit a tunable band gap, high absorption coefficient, longer carrier diffusion length, longer carrier lifetime, and high electron and hole mobilities [3]. Despite their excellent optoelectronic properties, 3D perovskites exhibit poor long-term stability when exposed to moisture, light, heat, and electric fields, hindering commercialization [4]. In comparison, two dimensional (2D) perovskites consist of hydrophobic organic spacer cation which controls ion migration and improves moisture and thermal stability, inhibiting its degradation [5]. Among the widely studied 2D perovskites, is the Ruddlesden-Popper (RP) phase of the form $A'_2A_{n-1}B_nX_{3n+1}$. Here, A'_2 represents a monovalent organic spacer cation such as phenethylammonium (PEA^+), butylammonium (BA^+) and fluorophenethylammonium cation ($FPEA^+$), A is an intralayer small cation such as caesium (Cs^+), methylammonium (MA^+) and formamidinium (FA^+), B is divalent cation such as Pb^{2+} and Sn^{2+}, X is a halide anion such as chloride (Cl^-), bromide (Br^-), and iodide (I^-), and n is the number of layers within inorganic sheets [6]. Pure 2D (n = 1) perovskites have been used independently or in mixed dimensional hybrid 2D/3D to improve the stability of solar cells, and LEDs [7].

The extensively studied low dimensional perovskites are lead (Pb)-based which raises toxicity and environmental concerns [2]. In contrast, tin (Sn)-based perovskites have shown great potential as prospective replacements for Pb-based counterparts [8]. Moreover, they exhibit excellent optoelectronic properties, and the ionic radii of Sn (118 p.m.) is similar to that of Pb (119 p.m.) [9]. However, Sn easily undergoes oxidation from Sn^{2+} to Sn^{4+} leading to detrimental Sn vacancies and impurities in Sn-based perovskite films [10]. In addition, the fast-crystallization of Sn-perovskites during solution processing induces residual strain resulting in poor quality films, affecting device

* Corresponding author
E-mail address: mmantsae.diale@up.ac.za (M. Diale).

https://doi.org/10.1016/j.vacuum.2024.113954
Received 7 June 2024; Received in revised form 21 November 2024; Accepted 14 December 2024
Available online 15 December 2024

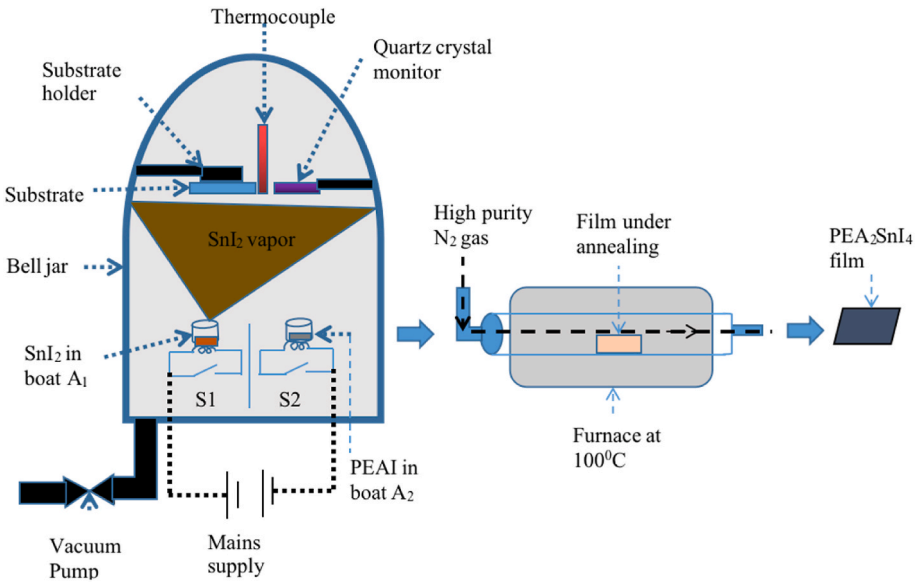

Fig. 1. Schematic showing the growth process of PEA_2SnI_4 perovskite thin films using SPVD and the annealing process.

performance [11].

Thermal evaporation is one of the well-established techniques that has been used to control crystallization in 3D Sn-perovskites, producing highly uniform thin films with good surface coverage [12]. It offers several advantages over solution-based methods such as ability to eliminate the use of toxic solvents, control over film thickness and yield good quality films [13,14]. The precursors are usually evaporated sequentially or co-evaporated (single-source or dual-source) to form perovskite films.

Yu et al. synthesized $MASnI_3$ perovskite thin films by co-evaporation of SnI_2 and MAI. They were able to control the crystallization of the resulting $MASnI_3$ perovskite by regulating the evaporation rate of SnI_2 precursor [15]. High quality films were produced with uniform surface coverage and good crystallinity. However, reproducibility was a problem since it was difficult to control the stoichiometry and thickness of the individual perovskite layers. La Place et al. reported the dual-source vacuum co-evaporation of 2D-PEA_2PbX_4 (X = I^-, Br^- or mixed I^- and Br^-) perovskite films [16]. The deposited 2D films exhibited a high degree of crystallinity at room temperature before annealing. However, they observed unavoidable halide cross-contamination in their deposition, suggesting a separate chamber for a given composition is necessary to improve the quality of the resulting films. Moreover, control of crystallization especially for Sn-based perovskites by co-evaporation may be difficult due to the fact that the perovskite precursors do not have the same physical and chemical properties.

On the contrary, SPVD offers the advantage of control over thickness of the individual layers which makes it more reproducible [17]. It is however noted that synthesis of 2D-Sn based perovskites by SPVD has rarely been explored, with a few of the available reports focusing on 3D Sn-based perovskites. Moghe et al. synthesized $CsSnBr_3$ perovskite thin film by sequentially evaporating multi-layers of CsBr and $SnBr_2$ with SnF_2 additive [18]. The solid-solid interaction of $SnBr_2$ and CsBr led to the production of films with good surface morphology and the resulting device exhibited an improved performance. Therefore, the extension of SPVD technique from 3D to 2D Sn-based perovskites integrated with crystallization control strategies can improve on reproducibility and the quality of the films.

In this study, 2D-RP PEA_2SnI_4 perovskite thin films were deposited by the SPVD. The effect of substrate temperature during the deposition, PEAI thickness, and annealing time on optical, morphological, and structural properties of the resulting 2D films was investigated. Lowering the substrate temperature below room temperature (~18 °C) helped to control SnI_2 crystallization before PEAI was subsequently evaporated. This ensured that the grain growth rate does not surpass the nucleation rate resulting into large grains with good surface coverage. Films deposited at low substrate temperatures exhibited higher PL intensities and longer carrier lifetime (0.56 ns) compared to those deposited at slightly high temperatures (0.14 ns). The optical, morphological and structural properties of the films were also observed to greatly depend on annealing time and PEAI thickness. To the best of our knowledge, there are no reports on the role of substrate temperature on the synthesis of 2D (n = 1) Sn-based perovskites by SPVD. This study suggests a way of improving the reaction of the 2D Sn-based precursors using SPVD by substrate temperature control. It also gives an insight into the effect of annealing and film thickness on the performance of 2D PEA_2SnI_4 films synthesized by the SPVD.

2. Experimental

Materials: SnI_2 (99.999 %) and PEAI (98 %) were obtained from Sigma Aldrich and used as received.

Substrate cleaning: FTO glass substrates of about 15 × 20 mm were cleaned using an ultrasonic bath with soap, acetone, isopropanol, and deionized water respectively for 15 min each. The substrates were then blow-dried with nitrogen gas and UV/ozone cleaned for 20 min.

PEA_2SnI_4 perovskite film deposition: Fig. 1 shows the deposition and annealing process of PEA_2SnI_4 perovskite thin films by SPVD. The resistive thermal evaporator chamber was first cleaned with extran solution to remove any possible contaminants. Clean glass/FTO substrates were mounted at a height of 22 cm from the boron nitride crucibles A_1 and A_2 containing SnI_2 and PEAI perovskite precursors, respectively. The chamber was evacuated to a pressure of 2×10^{-5} mbar and then SnI_2 was deposited (at a rate of 0.3 Å/s), followed by PEAI (at a rate of 1 Å/s). A quartz crystal monitor was used to measure the thickness of the films during the deposition. The thickness of SnI_2 was maintained at 100 nm while varying PEAI from 40 to 500 nm (40, 100, 300 and 500 nm). The temperature of the substrate was lowered to 18 and 25 °C by cooling and raised to 38 °C without cooling. Lowering the temperature of the substrate was achieved by placing ice sealed in a plastic bag at the top of the bell jar. The deposited films were then annealed at 100 °C in a furnace (Lindberg Hevi-duty tube furnace SB) with a continuous flow of high-purity nitrogen at a rate of 5 LPM. Annealing time was varied from 0 to 120 min (0, 20, 40, 60, 80 and 120 min).

Film characterization: XPERT-PRO X-ray diffraction (XRD)

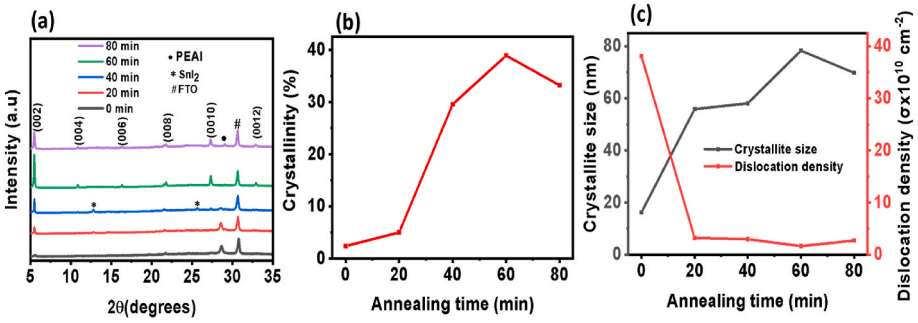

Fig. 2. (a) XRD diffractograms of the 2D PEA_2SnI_4 perovskite thin film with 500 nm PEAI thickness annealed at 100 °C for different times; (b) crystallinity; (c) crystallite size and dislocation density against annealing time for 500 nm PEAI thickness respectively.

spectrometer was used to characterize the structural properties of PEA_2SnI_4 perovskite films. 2θ was measured ranging from 5 to 35° in steps of 0.008 using Cu K-Alpha radiation source with wavelength of 1.5406 Å. The obtained spectra were used to study the structure, crystallinity, crystallite size, dislocation density and micro-strain by help of Origin Pro 2018 software. The optical absorption spectra of the films were obtained using ultraviolet–visible (UV–Vis) Cary 100 spectrometer within 300–800 nm wavelength range. Surface morphology of the films was studied using field emission scanning electron microscope (FE-SEM) Zeiss crossbeam 540. Grain size measurements on the obtained SEM images was performed using Image J software. FE-SEM Zeiss crossbeam 540 equipped with energy dispersive X-ray spectroscopy (EDS) system was used for EDS analysis on the surface of the films. The surface topologies were examined using WITech alpha300 RAS + atomic force microscope (AFM). Analysis on AFM images was performed using the WITec Suite FIVE software to obtain the root mean surface roughness and 3D topological images. Steady-state photoluminescence (PL) and time resolved photoluminescence (TRPL) spectra measurements were carried out using a confocal microscope (Ti-E Motorized Inverted Microscope, Nikon) with a 10 × /0.3NA (air) objective in an ambient environment. The lifetime measurements were performed using a supercontinuum pulsed laser with a pulse width of ≈67 ps and an average power of ≈836 nW operating at 20 MHz repetition rate (SuperK EVO, NKT Photonics) of which the excitation light was filtered to 525 nm wavelength (SuperK VARIA, NKT Photonics, 10 nm bandwidth). TRPL data acquisition was performed using a Becker & Hickl GmbH SPC-130 EM TCSPC module. The fourier transform infrared (FTIR) spectroscopy measurements were performed using JASCO FT/IR-4X spectrometer in transmission mode.

3. Results and discussion

3.1. Structural properties

3.1.1. Effect of annealing and PEAI thickness on structural properties of PEA_2SnI_4 thin films

Fig. 2(a) shows the XRD diffractograms of PEA_2SnI_4 perovskite thin films with 100 nm SnI_2 and 500 nm PEAI thickness annealed at 100 °C at different times. The crystal structure identified by XRD shows a typical 2D perovskite with characteristic peaks located at 00*l*; $l = 2$, 4, 6, 8, 10, and 12, corresponding to 2θ angles at 5.50°, 10.9°, 16.3°, 21.8°, 27.4° and 32.9°, respectively [19,20]. The d-spacing value of the PEA_2SnI_4 was calculated based on Bragg's law shown in equation (1) [21] and found to be 16.2 Å, in agreement with other reports [22].

$$n\lambda = 2dsin\theta \tag{1}$$

where n is an integer, λ is x-ray wavelength, d is crystal layers spacing (path difference) and θ is the incident angle (angle between the incident ray and the scatter plane).

It can be observed that after 60 min of annealing, all the peaks describing a 2D perovskite appeared, while the SnI_2 peak at $2\theta = 12.8°$ & 25.7° and PEAI peak at 28.7° disappeared, indicating that the perovskite was fully formed and the reaction was complete. The intensity of the major 2D peak at $2\theta = 5.50°$ increased with annealing time, implying that the perovskite crystal was oriented along the (002) plane [23]. During the deposition process, the substrate temperature was lowered to ~18 °C with the aim of keeping the first deposited SnI_2 layer nearly amorphous to facilitate an efficient interdiffusion process with the PEAI. The amorphous nature of SnI_2 increases the surface area for interaction with PEAI [24].

The appearance of 2D perovskite peaks upon annealing demonstrates that annealing was required to provide the activation energy needed for the interdiffusion of SnI_2 and PEAI to form the 2D perovskite. Annealing the perovskite film for 80 min resulted in a decrease in the intensity of the peaks and PEAI peak appeared at 28.7°, suggesting decomposition of the perovskite.

The crystallinity of the film was calculated using XRD data based on the integration method defined by equation (2) [25] in Origin Pro 2018 software.

$$\%crystallinity = \frac{Area\ under\ crystalline\ peaks}{Area\ under\ all\ peaks} \times 100. \tag{2}$$

Fig. 2(b) shows the plot of crystallinity of PEA_2SnI_4 against annealing time for the film with 500 nm PEAI thickness annealed at 100 °C. The degree of crystallinity was observed to increase steadily from 0 to 20 min, then sharply from 20 to 60 min attributed to an increase in grain size. Further annealing of the film from 60 to 80 min resulted into a decrease in crystallinity [26]. The crystallite size of the film was calculated based on the Williamson-Hall plot defined by equation (3) [27].

$$\beta\ cos\ \theta = \frac{k\lambda}{D} + 4\varepsilon\ sin\ \theta \tag{3}$$

where D is the diameter of the crystallite, λ is wavelength of the x-ray used (copper kα = 1.5406 Å), K is Scherrer's constant taken as 0.9 for spherical crystallites with cubic symmetry, ε refers to the macrostrain, β is the full wave at half maximum width (FWHM) and θ is half of the corresponding Bragg's diffraction angle. The dislocation density ρ, was

Table 1
Variation of crystallinity, crystallite size, dislocation density, micro-strain and average grain size with annealing time for PEA_2SnI_4 perovskite thin films.

Annealing time (min)	Crystallinity (%)	Crystallite size (nm)	Dislocation density (× 10^{10} cm^{-2})	Micro-strain (× 10^{-2})	Average grain size (nm)
0	2.40	16.2	38.1	13.7	92.52
20	5.01	55.9	3.20	0.390	253.2
40	29.6	58.1	2.97	0.120	340.3
60	38.9	78.3	1.63	0.190	453.1
80	33.2	69.8	2.71	0.151	398.7

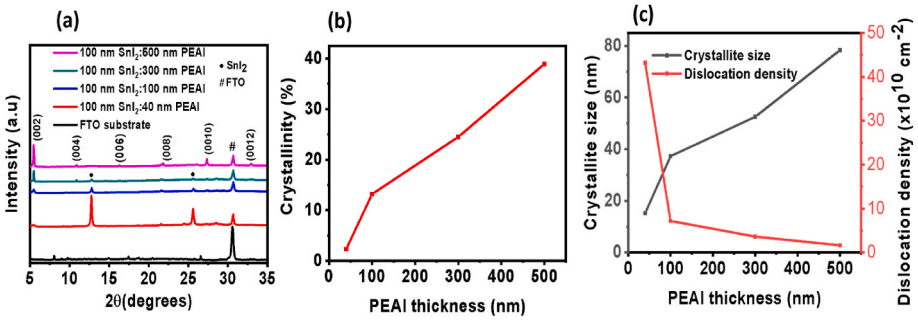

Fig. 3. (a) XRD spectra of the 2D PEA_2SnI_4 perovskite thin films for various PEAI thicknesses annealed at 100 °C for 60 min; (b) crystallinity; (c) crystallite size and dislocation density against PEAI thickness respectively.

Table 2
Variation of crystallinity, crystallite size, dislocation density, micro-strain and average grain size with PEAI thickness for PEA_2SnI_4 perovskite thin films.

PEAI thickness (nm)	Crystallinity (%)	Crystallite size (nm)	Dislocation density (× 10^{10} cm^{-2})	Micro-strain (× 10^{-4})	Average grain size (nm)
40	2.27	15.2	43.2	10.5	151.5
100	13.2	37.3	7.18	0.470	244.4
300	24.5	52.5	3.62	0.340	395.7
500	38.9	78.3	1.63	0.190	453.1

determined using the Williamson and Smallman formula shown in equation (4) [28]:

$$\rho = \frac{n}{D^2} \tag{4}$$

where n = 1 for minimum ρ and D is the crystallite size.

Fig. 2(c) and Table 1 show the variation of the crystallite size and dislocation density of 500 nm PEAI thickness film annealed at 100 °C at different times. The crystallite size of the film increased with annealing time (0–60 min) and then slightly decreased from 60 to 80 min, whereas an inverse trend was observed with dislocation density. The film annealed for 60 min showed the lowest dislocation density and largest crystallites suggesting low defects and trap states compared to the as-deposited film, which is beneficial for photovoltaic application [29]. Furthermore, Table 1 shows that the micro-strain decreased sharply upon annealing the film for 20 min. Annealing the film further resulted in a gradual decrease in micro-strain, which generally matched well with the increase in crystallite size.

The effect of PEAI thickness on the structural properties of the PEA_2SnI_4 was further investigated as shown in Fig. 3(a)–(c). Fig. 3(a) shows the XRD diffractograms of PEA_2SnI_4 films annealed at 100 °C for 60 min with varying PEAI from 40 to 500 nm. The SnI_2 peak at 2θ =

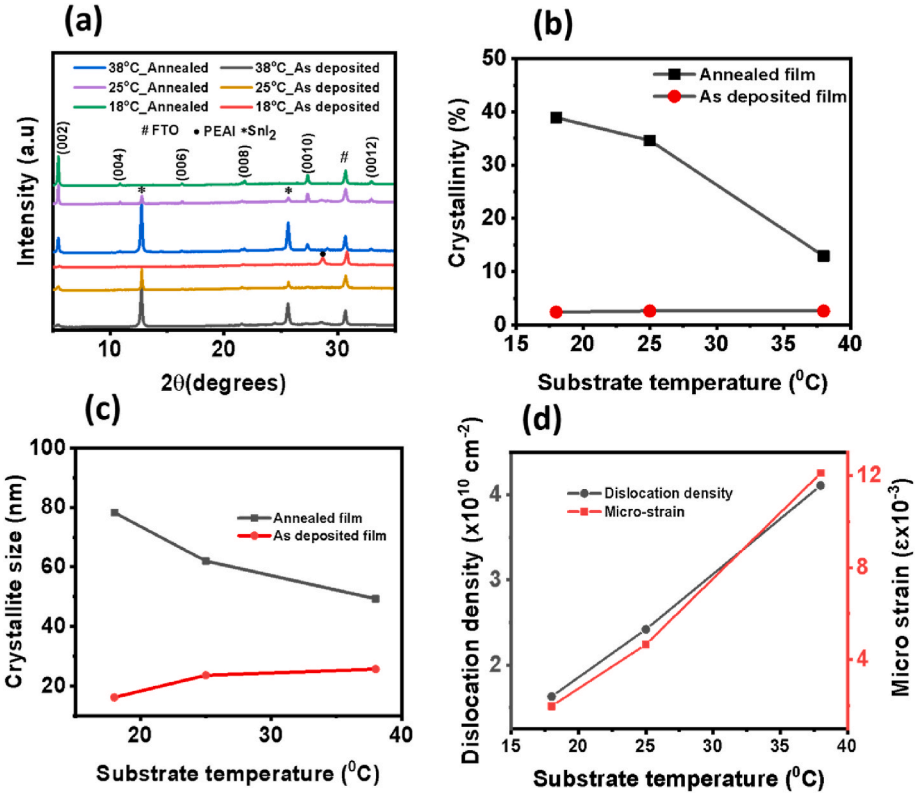

Fig. 4. (a) XRD spectra of the 2D PEA_2SnI_4 perovskite thin films with substrate temperature at 18, 25 and 38 °C during deposition; (b) crystallinity and (c) crystallite size against substrate temperature for as-deposited and annealed film; (d) Dislocation density and micro-strain against substrate for the films annealed at 100 °C for 60 min.

Table 3
Variation of crystallinity, crystallite size, dislocation density and average grain size with substrate temperature for as deposited and films annealed at 100 °C for 60 min.

Substrate temperature (°C)	Annealing time (min)	Crystallinity (%)	Crystallite size (nm)	Dislocation density ($\times 10^{10}$ cm^{-2})	Average grain size (nm)
18	0	2.35	16.24	35.15	92.52
	60	38.94	78.30	1.63	453.11
25	0	2.60	23.61	21.72	106.52
	60	34.6	62.3	2.42	332.84
38	0	2.61	26.71	14.03	170.63
	60	12.89	49.34	4.11	290.17

12.8° and 25.7° reduced with an increase in PEAI thickness, which disappeared completely at 500 nm, indicating a complete reaction. Therefore, the phase quality of PEA_2SnI_4 perovskite thin film improved with increase in PEAI thickness. Furthermore, the 2D perovskite peaks at (002), (004), (006), (008), (0010) and (0012) became more prominent with increasing PEAI thickness attributed to enhanced perovskite formation and reduction of residual SnI_2 [30]. Similarly, the degree of crystallinity was observed to increase with PEAI thickness as shown in Fig. 3(b). Fig. 3(c) shows the variation of dislocation density and crystallite size with PEAI thickness. A high dislocation density at 100 nm SnI_2: 40 nm PEAI (lower PEAI thickness) could be due to the existence of residual SnI_2. Increasing PEAI thickness to 100 nm reduced the dislocation density sharply as small traces of residual SnI_2 could be observed. Excess SnI_2 in the film has been proven to be at times beneficial in the formation of 3D/2D perovskites [31] or to have negative impact on the crystallization of the films, resulting into poor film morphology [32]. These observed variations in dislocation density agree with the changes in crystallite sizes.

The micro-strain was also observed to decrease as PEAI thickness rose from 40 to 500 nm as depicted in Table 2. The high micro-strain observed at 40 nm PEAI thickness could be due to the presence of high residual SnI_2 amounts in the film as observed from XRD in Fig. 3(a) and the reduced crystallite sizes [33,34].

3.1.2. *Effect of substrate temperature on structural properties of PEA_2SnI_4 thin films*

The effect of substrate temperature on perovskite formation was investigated by lowering the substrate temperature below room temperature (25 °C) to ~18 °C (by cooling) and raising it above room temperature to ~38 °C (without cooling) during deposition as depicted in Fig. 4(a). No 2D PEA_2SnI_2 and SnI_2 peaks were observed in the as-deposited film at 18 °C, suggesting that no reaction took place between the perovskite precursors and SnI_2 did not crystallize during deposition in the chamber. Keeping the SnI_2 layer nearly amorphous before the introduction of the PEAI increases the surface area of interaction between the perovskite precursors [32]. All the 2D perovskite peaks at a low substrate temperature appeared only after the film was annealed, suggesting that annealing provided the activation energy needed for the interdiffusion of PEAI into SnI_2 to form pure 2D PEA_2SnI_4 perovskite. On the other hand, the XRD diffractograms for the as-deposited film at room temperature and at a raised substrate temperature (38 °C) exhibited sharp peaks of SnI_2, which was attributed to its fast crystallization at a slightly high temperature. These films showed low-intensity 2D perovskite peaks after annealing. Furthermore, it retained a high intensity of SnI_2 peaks, implying that the SnI_2 continued to crystallize and all of it did not react sufficiently with PEAI leaving residual SnI_2 in the film.

Fig. 4(b) and Table 3 show the variation of crystallinity of PEA_2SnI_4 film with substrate deposition temperature. The film grown at a low substrate temperature exhibited a high degree of crystallinity. On the other hand, the 38 °C substrate temperature resulted in low crystallinity due to enhanced stacking fault in the film [35] for both the as-deposited and annealed films. It can be observed from Fig. 4(c) that the as-deposited films at all substrate temperatures exhibited small crystallite sizes. Annealing greatly improved the crystallite sizes and it was observed to decrease with increase in substrate temperature. The film grown at 18 °C displayed the largest crystallites attributed to crystallization control of SnI_2 which favoured grain growth [35]. It can be observed in Fig. 4(d) that low substrate temperature deposition is associated with low dislocation density and reduced micro-strain further attributed to enlarged crystallites and the high film quality.

To further investigate the effect of substrate temperature on the degree of crystallization of SnI_2, XRD measurments were carried out on the as-deposited SnI_2-only films grown at substrate temperatures of 18, 25 and 38 °C as shown in Fig. S2. SnI_2-only films deposited with substrate temperature at 18 °C revealed a broad and very low intensity peaks, indicating very low crystallinity (neary amorphous). On the other hand, SnI_2 films deposited at 25 and 38 °C exhibited high intense and narrow (001) and (002) crystalline peaks, demonstrating high degree of crystallinity in agreement with the XRD results in Fig. 2(a). Thus suggesting the need to reduce the substrate temperature below room temperature (25 °C) during deposition in order to control SnI_2 fast crystallization. The crystallization of SnI_2 at an excessively high temperature was further investigated by post-annealing treatment at 100 °C to assess its effect on perovskite formation. It is observed in Fig. S2 of supporting document information that the crystallinity of the SnI_2 film greatly increased at an excessively high temperature (100 °C). The highly crystalline SnI_2 layer will hinder its interdiffusion with the second sequentially deposited precursor, affecting perovskite growth. Similar findings of poor perovskite formation at a high substrate temperature has been reported by Zhang et al. using solution processing methods attributed to aggregartion of the nuclei leading to formation of islands [36]. On the other hand extremely low substrate temperatures have been reported by Lohmann et al. to greatly improve grain growth during co-evaporation process of 3D perovskites [37]. Their results revealed extremely low substrate temperatures of −2 °C led to micrometer-sized grains while room temperature (23 °C) led to small sized grains (only a few nanometers). They attributed the difference in grain sizes to adsorption rate dependence on substrate temperature. However, unlike co-evaporation, with sequential evaporation process, we attribute the observed difference in the grain growth to not only the adsorption rate but also to the crystallization kinetics-substrate temperature depedence of the first SnI_2 precursor layer.

3.2. *Optical properties*

3.2.1. *Effect of annealing and PEAI thickness on the optical properties of PEA_2SnI_4 thin films*

Fig. 5(a) and (b) show the UV–vis absorption spectra of 2D (n = 1) PEA_2SnI_4 perovskite thin films subjected to different annealing times. The films exhibited three absorption peaks assigned to intrinsic exciton absorption of the formed quantum well structure (607 nm), charge transfer transition between organic spacer cations and inorganic layers (525 nm), and high energy exciton transition (416 nm) which agrees with the literature [38,39]. The absorption peaks increase with annealing time from 0 to 60 min, consistent with the intensity of the XRD peaks in Fig. 2(a), and then decreases upon long time annealing of 120 min.

A red shift in absorption onset was observed when annealing the film from 0 min (628 nm) to 60 min (636 nm) and a blue shift for the film

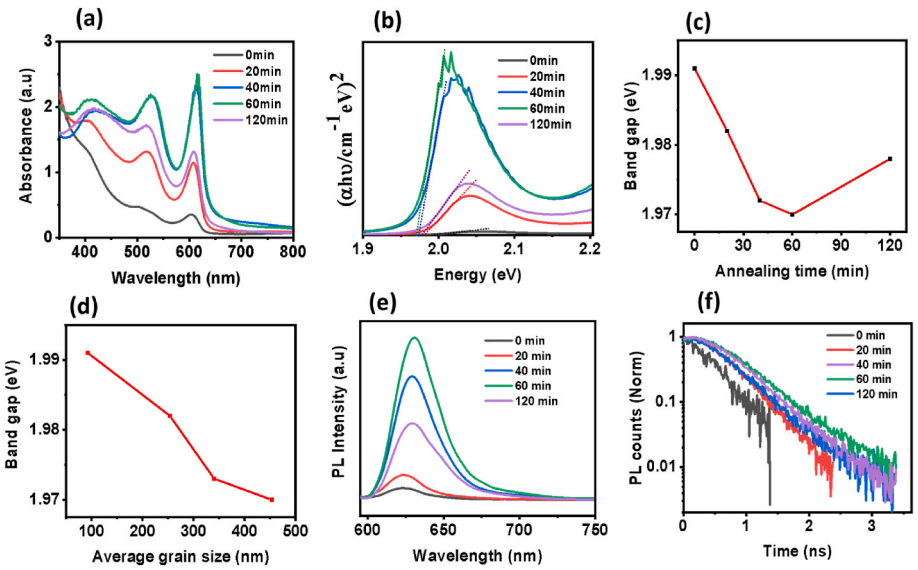

Fig. 5. (a) UV–Vis absorption spectra; (b) Tauc-plot; (c) and (d) variation of bandgap with annealing time and average grain size respectively; (e,f) PL and TRPL spectra of 2D PEA_2SnI_4 perovskite films annealed for different times at 100 °C with film thickness of 100 nm SnI_2:500 nm PEAI.

Table 4
TRPL carrier lifetime of PEA_2SnI_4 thin films for different annealing times.

Annealing time (min)	τ_1 (ns)	τ_2 (ns)	τ_{avg} (ns)
0	0.06	0.32	0.12
20	0.39	0.39	0.39
40	0.48	0.49	0.47
60	0.56	0.56	0.56
120	0.46	0.46	0.46

annealed for 120 min (632 nm), consistent with the bandgap results in Table S1 in supporting information determined from the Tauc-plot in Fig. 5(b). The band gap decreased from 1.991 to 1.970 eV for 0–60 min of annealing time, respectively. However, further annealing of the film for 120 min, led to an increase in the band gap as shown in Fig. 5(c). The decrease in band gap for 0–60 min of annealing time is attributed to the increase in grain sizes resulting from tensile strain in the film as shown in Fig. 5(d) [40].

PL and TRPL measurements shown in Fig. 5(e) and (f), respectively were carried out to further examine the effect of annealing on the optical properties of the films. A red shifting of the emission peak was observed when the film is annealed from 0 to 60 min and a blue shifting at 120 min, which is consistent with the UV–Vis absorption results. The corresponding emission peaks were at ≈623, 625, 629, 631 and 629 nm for 0, 20, 40, 60 and 120 min of annealing time, respectively. In addition, the PL peak intensity increases with annealing from 0 to 60 min, suggesting the reduction of trap states and grain boundaries [41]. The trap states act as nonradiative recombination centers whereas a large number of grain boundaries can lead to oxygen and moisture permeation into the film, inducing Sn^{2+} oxidation. On the other hand, the low PL peak intensity at 120 min, is attributed to prolonged annealing which damages the film. Table 4 and Fig. 5(f) show that the average carrier lifetime of

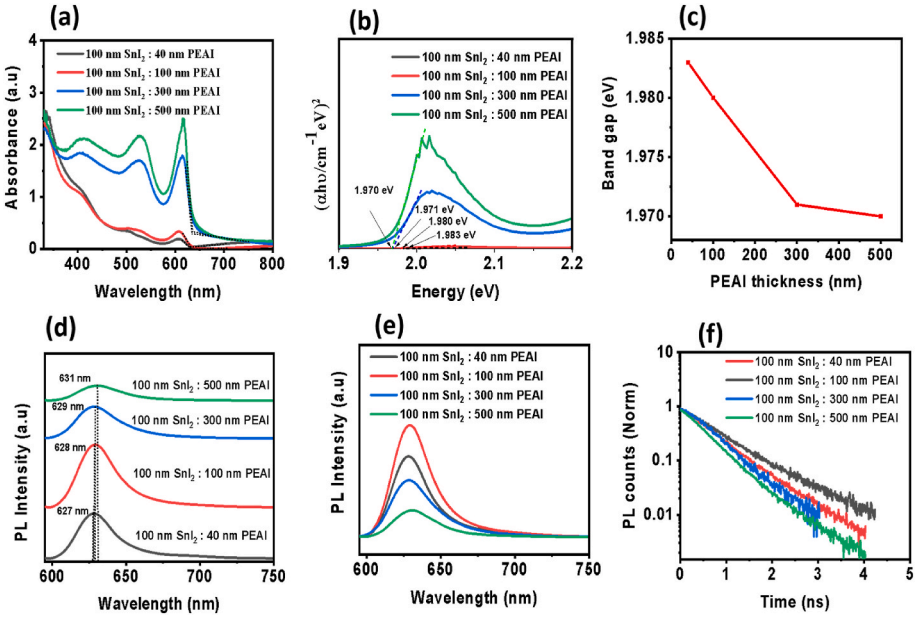

Fig. 6. (a) UV–Vis absorption spectra; (b) Tauc-plot; (c) variation of bandgap of PEA_2SnI_4 thin films with PEAI thicknesses; (d,e) PL spectra showing shift in peak intensities and peak intensity variations respectively; (f) TRPL spectra of 2D PEA_2SnI_4 perovskite thin films deposited with varying PEAI thicknesses.

Table 5
TRPL carrier lifetime of PEA_2SnI_4 thin films for varying PEAI thicknesses.

PEAI thickness (nm)	τ_1 (ns)	τ_2 (ns)	τ_{avg} (ns)
40	0.40	0.90	0.58
100	0.42	1.08	0.63
300	0.50	0.57	0.55
500	0.31	0.74	0.39

the films improved with annealing time from 0.12 to 0.56 ns, which further confirms the reduction of defect density and grain boundaries within the films. The shorter carrier lifetime at 120 min, indicated that prolonged annealing created defects in the film, consistent with SEM results in supporting information document (Fig. S4(b)).

UV–vis absorption, PL and TRPL spectra measurements were further carried out to assess the effect of PEAI thickness on optical properties of PEA_2SnI_4 thin films. Fig. 6(a), shows the UV–Vis absorption spectra of 2D PEA_2SnI_4 perovskite films with fixed 100 nm SnI_2 but varying PEAI thickness from 40 to 500 nm. It is observed that for smaller PEAI thickness, the absorption almost mimics that of SnI_2 film (Fig. S3 of supporting information) with low 2D absorption peak intensities. This implies that a very thin layer of 2D PEA_2SnI_4 was formed leaving excess unreacted SnI_2 as confirmed by XRD diffractogram in Fig. 3(a). The formed thin 2D layer is good for 3D perovskite layer capping to suppress degradation of the perovskite for solar cell applications [31]. Furthermore, absorption is seen to increase with PEAI thickness from 40 to 500 nm with a red shift in the absorption onset. The high absorption exhibited by large thickness 2D perovskites (>300 nm) has been used for other applications such as photodetectors, LEDs, and Field-effect transistors despite their poor conductivity [41,42]. It is observed in Fig. 2(b) and (c) (also in Table S2) that the band gap decreases from 1.983 to 1.970 eV as the thickness of PEAI increased from 40 to 500 nm respectively attributed to the increase in crystallite size as shown in Fig. 3(c) [43,44].

The steady state PL spectra in Fig. 6(d) show a slight redshift of peak intensity as the PEAI thickness increased, which agrees with the observed small variations in the band gap in Fig. 6(c). A much stronger PL intensity was displayed when PEAI thickness increased from 40 to 100 nm as shown in Fig. 6(e). Further increase of PEAI thickness to 300 and 500 nm resulted in lower PL intensities. This implies that 100 nm PEAI thickness resulted in a film with suppressed nonradiative carrier recombination compared to thicker films. This was further confirmed by the longer carrier lifetime of 0.63 ns for 100 nm PEAI thickness film compared to 0.39 ns for 500 nm PEAI thickness film observed from the TRPL results in Fig. 6(f) and Table 5. This could be due to the low carrier mobility and short diffusion length characteristics of layered 2D perovskites which make thicker films more susceptible to charge carrier recombination [45].

3.2.2. *Effect of substrate temperature on the optical properties of PEA_2SnI_4 perovskite thin films*

Fig. 7(a) shows the UV–Vis absorption spectra of PEA_2SnI_4 perovskite thin films with substrate temperature at 18, 25 and 38 °C. A low UV–Vis absorption is observed for the as-deposited films at all substrate temperatures. However, the annealed film deposited at 18 °C substrate temperature showed a high optical absorption compared to that deposited at 25 and 38 °C. This was attributed to the nearly amorphous nature of the SnI_2 layer which provided a good surface area for interaction between the inorganic and the organic layers forming a good quality film with high crystallinity, full surface coverage and enlarged grains after annealing [24,46]. The band gap band determined using the Tauc-plot equation at different substrate temperatures is shown in Table S3 of supporting document. The estimated band gaps for the annealed films increased from 1.970 to 1.972 eV as the substrate temperature increased from 18 to 38 °C as shown in Fig. 7(b). The small band gap observed at 18 °C is attributed to the increased grain sizes compared to that at 38 °C.

PL and TRPL spectra were further measured to compare the carrier dynamics of the films deposited with the substrate held at 18, 25 and 38 °C as shown in Fig. 7(c) and (d) respectively. PL peak intensities for all the as-deposited films are lower than for the annealed films, further indicating the importance of annealing in suppressing defect density. The highest PL peak intensity and longest carrier lifetime (0.56 ns) was obtained with the annealed film deposited at a substrate temperature below room temperature as shown in Fig. 7(d) and Table 6. This suggests that reducing the substrate temperature minimized defect density, hence greatly suppressing nonradiative recombination within the film. The low defect density at low substrate temperatute is attributed to the controlled crystallization and grain growth, resulting into high quality

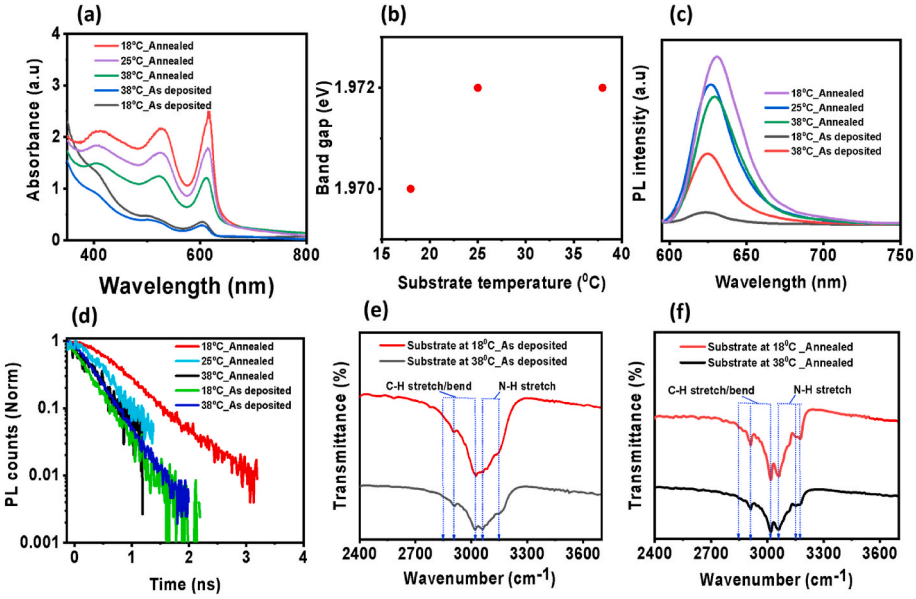

Fig. 7. (a) UV–Vis absorption spectra of 2D PEA_2SnI_4 perovskite films with substrate held at 18, 25 and 38 °C during deposition; (b) variation of bandgap of PEA_2SnI_4 films with temperature of the substrate; (c,d) PL and TRPL spectra respectively for the resulting films; (e,f) FTIR transmission spectra for as-deposited and annealed films respectively at substrate temperature of 18 and 38 °C.

Table 6
TRPL carrier lifetime of PEA_2SnI_4 thin films at different substrate temperatures.

Substrate temperature (°C)	Annealing temperature (°C)	τ_1 (ns)	τ_2 (ns)	τ_{avg} (ns)
18	0	0.06	0.32	0.08
	60	0.56	0.56	0.56
25	60	0.29	0.42	0.34
38	0	0.07	0.37	0.12
	60	0.12	0.39	0.14

films.

FTIR transmission spectra measurements were carried out on PEA_2SnI_4 perovskite thin films grown at different substrate temperatures to understanding the chemical interactions between the perovskite precursors and the effect of the synthesis environment for any possible residual water vapor contaminations. The FTIR spectra measured in the range 2400–3700 cm^{-1} for as-deposited films at 18 and 38 °C in Fig. 7(e) displayed peaks at 2846.8, 2908.3 and 3018.1 cm^{-1} belonging to either asymmetric or symmetric C-H stretching or bending bond vibrations. The peaks located at 3062.7 and 3152.8 belong to N-H stretching vibrations which agrees with literature [28]. It was observed that the as-deposited films exhibit weak intensities of the peaks, further confirming the poor interection between the perovskite precursors before the annealing process. It is worth noting that no characteristic peak in the range 3400–3700 cm^{-1} corresponding to O-H stretching vibrations was observed in all the films. This suggested that the cooling synthesis environment did not result in residual water vapor contaminations that would impenge the perovskite film. Fig. 7(f) shows the FTIR measurements for annealed films at the different substrate temperatures. The annealed films displayed higher peak intensities compared to as-deposited films. Further more, the film deposited with substrate temperature at 18 °C displayed more intense peaks compared to that at 38 °C, further suggesting the role of substrate temperature deposition in the interaction process of the perovskite precursors.

3.3. Morphological properties

3.3.1. Effect of annealing and PEAI thickness on the surface morphology of PEA_2SnI_4 thin films

FE-SEM was used to study the morphology of the as-deposited and annealed PEA_2SnI_4 films at different annealing times as shown in Fig. 8 (a–d). The as-deposited film exhibited small and non-compact grains as shown in Fig. 8(a). However, when the film was annealed, platelets consisting of multiple grains started forming whose compactness improved with increasing annealing time as shown in Fig. 8(b–d) [47]. The small and non compact grains for the as-deposited film is attributed

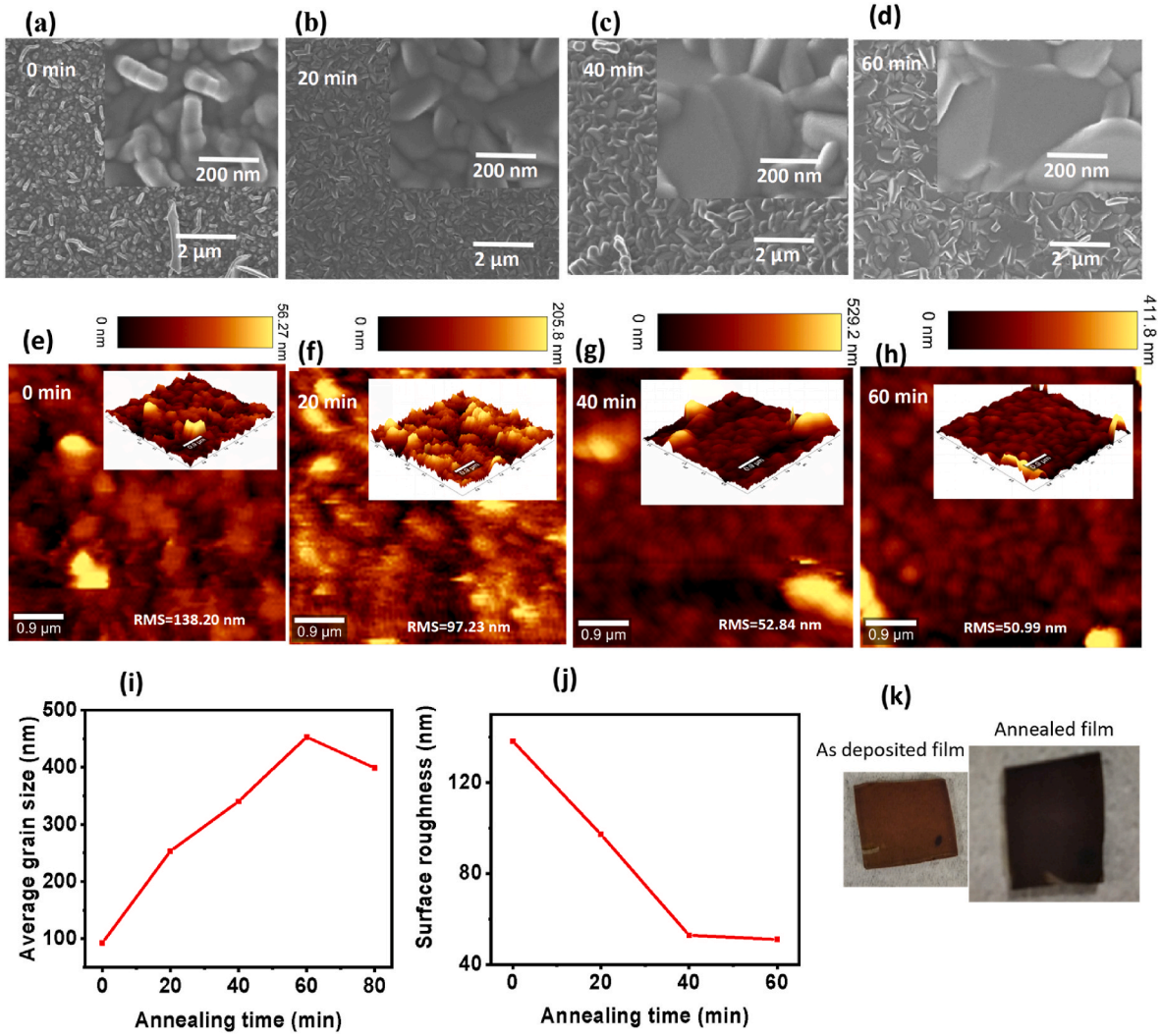

Fig. 8. (a–d) FE-SEM images of PEA_2SnI_4 Perovskite thin films at different annealing times. The inset indicates the magnified view of crystalline grains in the film; (e–h) AFM images for the films at different annealing time. The inset shows 3D lateral images of the films; (i) and (j) variation of average grain size and surface roughness, respectively with annealing time; (k) photo showing appearance of as-deposited and annealed films.

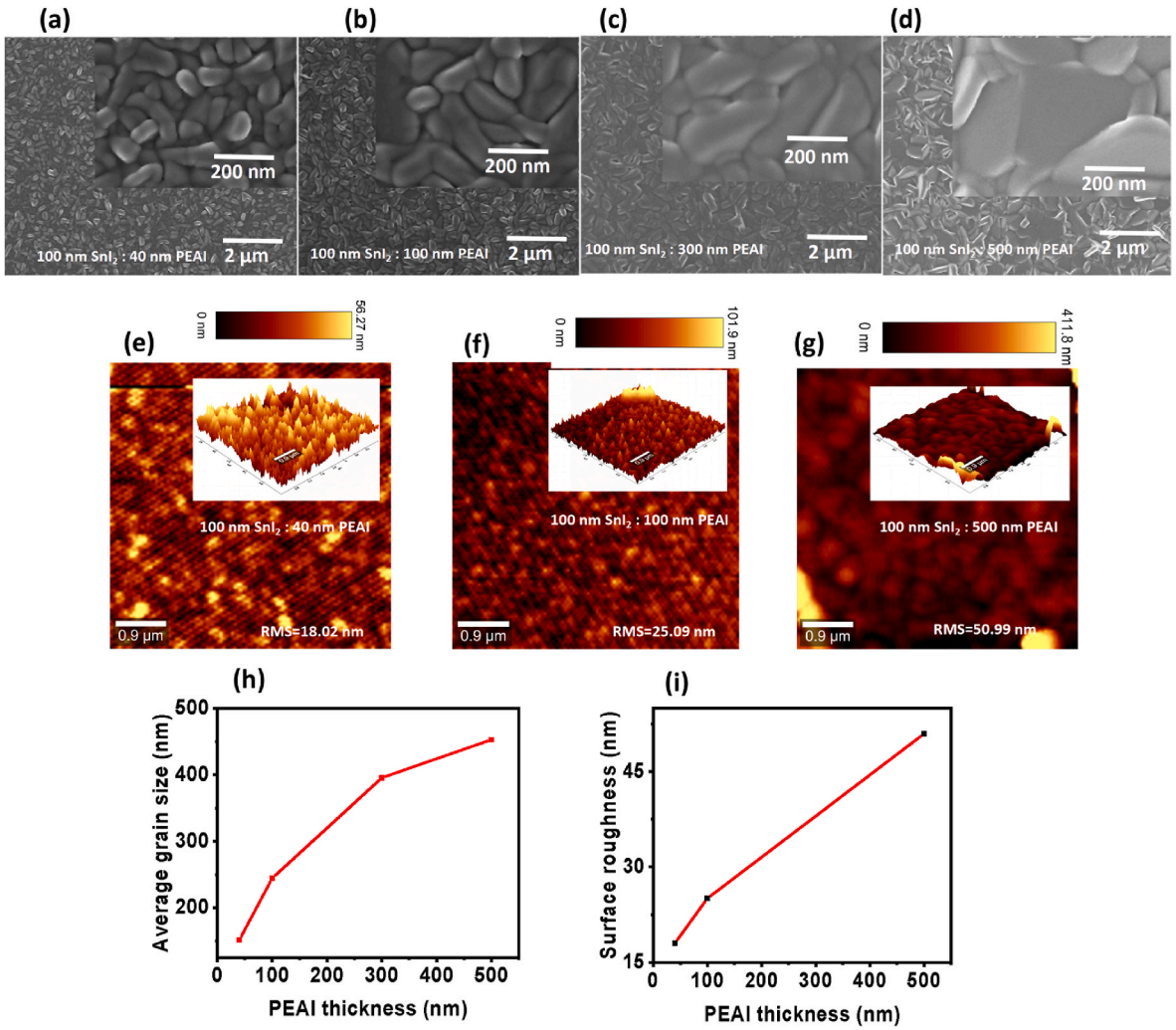

Fig. 9. (a–d) FE-SEM images of PEA_2SnI_4 perovskite thin films with varying PEAI thicknesses of 40, 100, 300 and 500 nm respectively. The inset indicates the magnified view of crystalline grains in the film; (e–g) AFM images for different PEAI thicknesses of 40, 100 and 500 nm respectively. The inset shows 3D lateral images of the films; (h) and (i) variation of average grain size and surface roughness, respectively with PEAI thickness.

to presence of PEAI at the surface of the film, due to poor interdiffusion process of the perovskite precursors. An improvement of film surface coverage and reduction of grain boundaries was observed with increase in annealing time attributed to better crystallization of the 2D perovskite in agreement with increasing intensity of XRD peaks in Fig. 2(a). The estimated average grain sizes were 92.52, 253.2, 340.3, 453.1 and 398.7 nm corresponding to 0, 20, 40, 60, and 80 min of annealing time respectively as shown in Table 1. The observed trend of increase in average grain size with annealing time as shown in Fig. 8(i) was attributed to better interdiffusion process occurring between perovskite precursors [48]. It can be observed that annealing the film for 80 min resulted in reduction of average grain size (Fig. S4(a)) and extended annealing time of 120 min (Fig. S4(b)) led to grain destruction.

AFM was used to further analyze the effect of annealing on the morphology of the films. Fig. 8(e–h) shows AFM images of as-deposited and films annealed for 20, 40 and 60 min with corresponding measured root mean square roughness (RMS) of 138.2, 97.23, 52.84, and 50.99 nm respectively. It can be observed that RMS decreases with increase in annealing time (Fig. 8(j)). The generally observed high RMS values could be attributed to the highly oriented crystal structure nature of the 2D perovskites. Additionally, the high reactivity and affinity of the precursors could result in the grain growth rate occurring faster than the nucleation rate, producing films with high surface roughness [47]. The color image of the films in Fig. 8(k) shows that brownish color of the as-deposited film turned dark upon annealing suggesting a transformation from SnI_2-rich to SnI_2-deficient perovskite film.

FE-SEM was used to investigate the influence of PEAI thickness on the morphology of PEA_2SnI_4 thin films as shown in Fig. 9(a–d). The insets represent a magnified view of the SEM images. It can be observed in Fig. 9 (a), that the film with 40 nm of PEAI is smooth with smaller grains which could be attributed to excess SnI_2. As PEAI thickness increased, grain growth improved and platelets made up of multiple grains were observed particularly for large PEAI thicknesses as shown in Fig. 9(c) and (d). The estimated average grain sizes were 151.5, 244.4, 395.7, and 453.1 nm corresponding to 40, 100, 300 and 500 nm of PEAI thicknesses as shown in Table 2. It is however observed that the average grain size of the films grown by SPVD technique is smaller than the solution-processed PEA_2SnI_4 perovskites which is of a few micrometers. This is attributed to the substantial morphological advancements in solution-processing techniques which involve the use of solvents such as dimethylsulfoxide (DMSO) and other additives which slown down the reaction rates and control the crystal growth resulting into large grain sizes. The average grain size increased with PEAI thickness as observed in Fig. 9(h). The grain size dependence behavior on thickness is consistent with the trend observed in 2D Pb-based perovskites prepared by drop-casting [49]. Despite the enlarged grains exhibited by thicker 2D perovskites, they have been found to badly affect the solar cell parameters thus suitable for other application such as photo detectors and

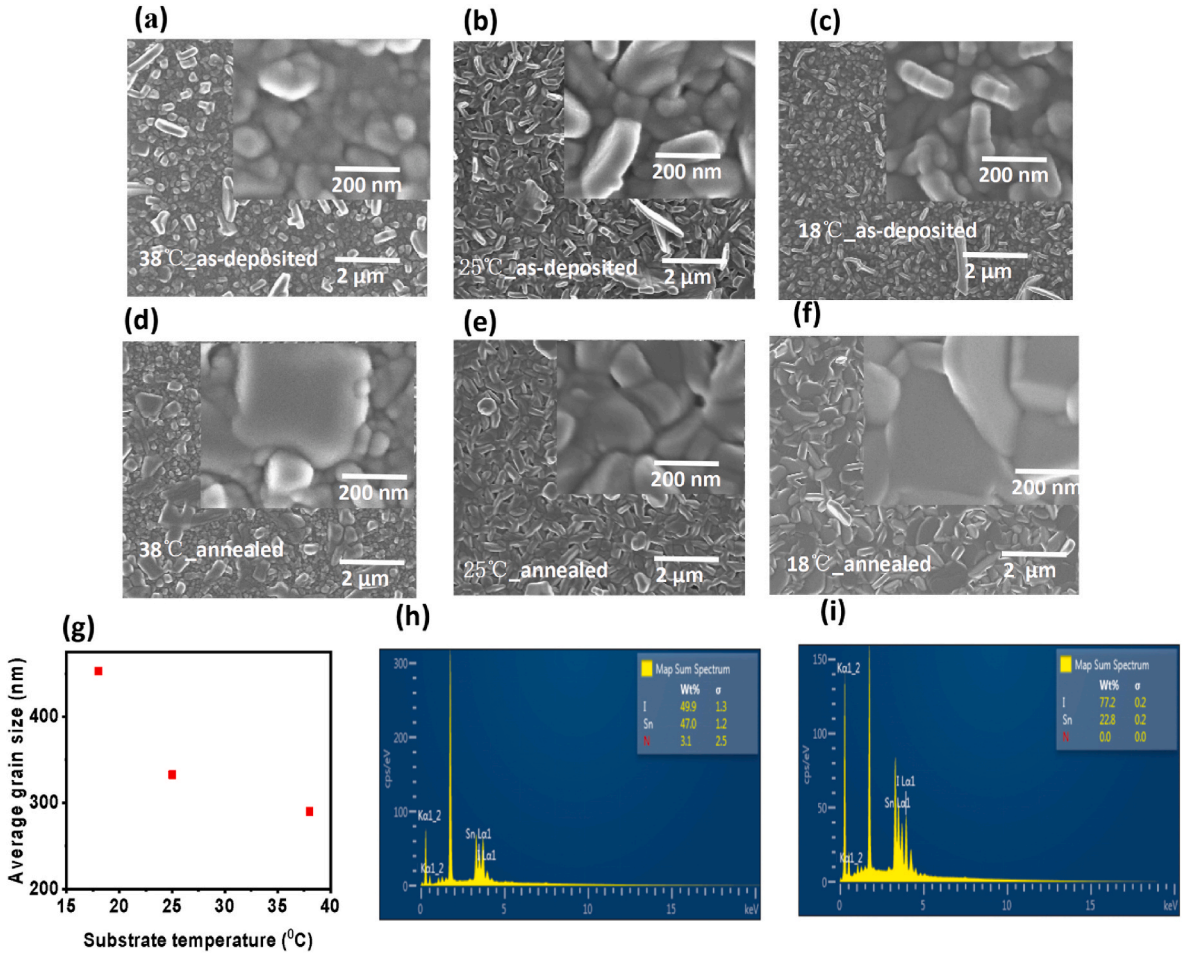

Fig. 10. FE-SEM images of as deposited and annealed PEA_2SnI_4 perovskite thin films at a substrate temperature of (a,d) 38; (b,e) 25 and (c,f) 18 °C; (g) variation of average grain size with substrate temperature for annealed films; (h,i) EDS spectra acquired in SEM at the surface of annealed films at 38 and 18 °C substrate temperatures respectively.

LEDs.

Fig. 9(e–g) shows AFM images of PEA_2SnI_4 films and the corresponding 3D lateral images as insets for varying PEAI thicknesses of 40, 100 and 500 nm. The calculated RMS values were 18.02, 25.08 and 50.99 nm for 40, 100 and 500 nm of PEAI thickness respectively. It can be observed from Fig. 9(i) that the surface roughness increases with PEAI thickness. The low surface roughness for smaller PEAI thickness of 40 nm further confirms the suitability of thinner 2D perovskites as a capping layer for 3D perovskites and providing a good interface with hole transport layers (HTLs) or electron transport layers (ETLs). The higher surface roughness exhibited at 500 nm of PEAI thickness could be due to formation of large platelets of which some are seen to be oriented vertically.

3.3.2. Effect of substrate temperature on surface morphology and stoichiometry of PEA_2SnI_4 thin films

SEM images of as-deposited and annealed films with slightly low substrate temperature (18 °C), room temperature (25 °C) and slightly high temperature (38 °C) are shown in Fig. 10(a–f) with insets representing the magnified view of the crystalline grains. The as-deposited film at 38 °C exhibits poor surface coverage with small grains as illustrated in Fig. 10(a). Upon annealing the film, a non-uniform grain growth with the film dominated by several small grains was observed as shown in Fig. 10(d). In addition, the film showed a characteristic of fast grain growth from a few nucleation sites leading to formation of voids attributed to the fast crystallization of SnI_2 before interdiffusion with PEAI rendering reduced nucleation sites [50]. On the other hand, the as-deposited film in Figure (b) and (c) at a lower substrate temperature (25 and 18 °C) exhibited small and randomly oriented grains which resulted into platelets consisting of closely packed enlarged grains upon annealing as shown in Fig. 10(e) and (f).

The average grain size greatly increased from 290.2 nm to 453.1 nm as the substrate temperature reduced from 38 to 18 °C as shown in Fig. 10(g) and Table 3. Lowering the substrate temperature below room temperature slowed down SnI_2 crystallization during deposition which helped to ensure that grain growth does not surpass the nucleation rate resulting into large grains with good surface coverage. To further understand the effect of substrate temperature on morphology of SnI_2, FE-SEM images of the SnI_2-only film subjected to different temperatures were obtained as shown in Fig. S5 of the supporting information document. It is observed that the SnI_2-only film with substrate temperature held at low temperature (18 °C) shows small and poorly distinct grains further confrming its poor crystallization which agrees with XRD results. The film at 25 °C is more crystalline with distinctive and enlarged grains compared to that at 18 °C which further confirms the advantages of having to lower the substrate temperature below room temperature for efficient SnI_2-PEAI interdiffusion process. Films deposited at 38 °C show clear, large and fully crystallized grains. The large grains and highly crystalline film exhibited by the SnI_2-only film at 38 °C affect PEAI interdiffusion. On the other hand, the film at an excessively elevated temperature of 100 °C (Fig. S5(d) of supporting information document) resulted into more compact and enlarged grains compared to all the low substrate temperature SnI_2-only films which is more likely to hinder the interdiffusion between the inorganic and the organic perovskite

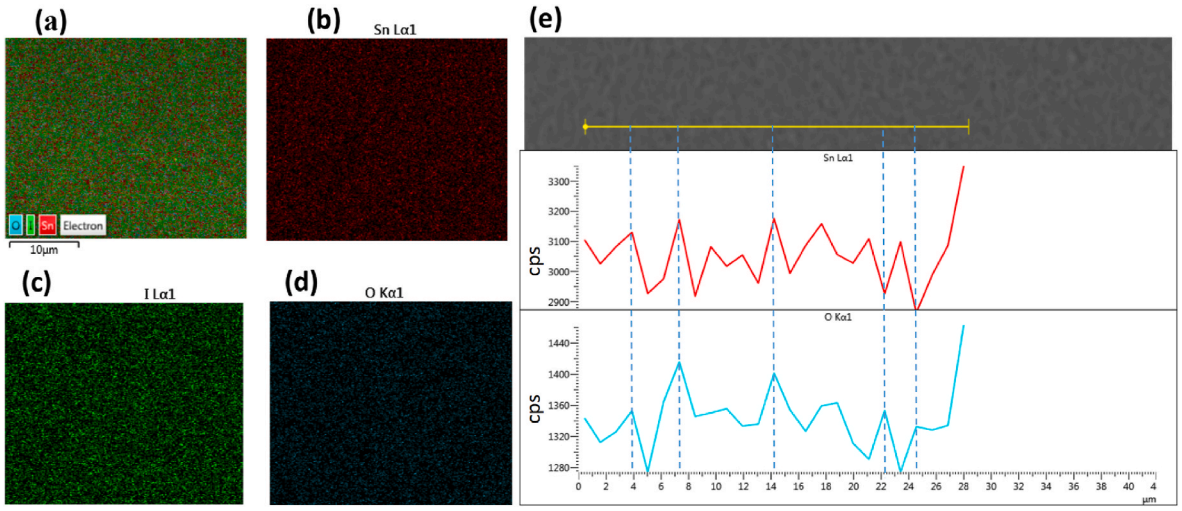

Fig. 11. (a)–(d) EDS elemental mapping showing the distribution of Sn, I and O for PEA_2SnI_4 perovskite annealed thin films with the substrate temperature at 18 °C; (e) SEM image with the corresponding Sn and oxygen counts from EDS elemental mapping along the marked yellow line. All images were taken at 10 μm magnification.

precusors.

Fig. 10(h) and (i) shows the Sn and I elemental compositions of annealed PEA_2SnI_4 perovskite thin films deposited on FTO-coated glass substrates held at 38 °C and 18 °C, respectively measured by energy dispersive X-ray spectroscopy (EDS). The estimated atomic ratios of Sn:I from the inset of Fig. 10(h) and (i) are 0.94 and 0.29 at substrate temperatures of 38 and 18 °C respectively. It can be observed that the ratio of Sn:I for a low substrate temperature is much closer to the stoichiometry of the PEA_2SnI_4 (0.25), than when the substrate is held at a slightly higher temperature. This indicates that low substrate temperatures favoured the formation of pure-phase PEA_2SnI_4 perovskite by SPVD.

Fig. 11(a–d) shows the EDS elemental mapping (including oxygen) for PEA_2SnI_4 thin films grown with the substrate temperature at 18 °C. It was observed that the elements Sn and I are uniformly distributed with traces of oxygen which could be as a result of exposure to air during preparations of the films for measurements. Moreover, majority of the oxygen is seen to segregrate at the Sn site on the grain interface as shown in Fig. 11(e). Sn perovskites are known to easily get oxidized from Sn^{2+} to Sn^{4+} in presence of oxygen and moisture, thus the high concetration of oxygen at the Sn site could be the source of fast degration of the perovskite. Some oxygen is also seen at the grain boundaries which act as permeation centers for deep penetration into the film. It should be noted that low magnifications were used during EDS elemental mapping measurments due to high sensitivity of the films, thus contributing to the low observed counts.

4. Conclusion

We fabricated Ruddlesden-Popper PEA_2SnI_4 perovskite thin films from SnI_2 and PEAI precursors using SPVD. Substrate deposition temperature, PEAI thickness and annealing time were found to have a notable influence on optical, morphological and structural properties of the resulting films. The temperature of the substrate during deposition was lowered slightly below room temperature (~18 °C) to control SnI_2 crystallization before the second precursor (PEAI) was subsequently evaporated. As a result, there was efficient interdiffusion process between the perovskite precursors after annealing, resulting into pure phase PEA_2SnI_4 perovskite film with high degree of crystallinity and suppressed nonradiative recombination. Lowering the substrate temperature ensured that grain growth does not surpass the nucleation rate which resulted into large grains with good surface coverage. XRD results revealed an increase in crystallinity and crystallite size with PEAI thickness while dislocation density and micro-strain decreased with PEAI thickness. The film with 40 and 100 nm PEAI thickness exhibited a higher PL intensity compared to thicker 300 and 500 nm PEAI films, demonstrating more nonradiative recombination in large thickness 2D films. AFM results showed that RMS decreased with increase in annealing while an inverse trend was observed with PEAI thickness. The findings of this work demonstrate the potential of using SPVD to deposit 2D Sn-based perovskites capable of being used as a capping layer for 3D perovskites or other optoelectronics applications and emphasizing the role played by substrate deposition temperature, film thickness and annealing towards crystallization dynamics of the perovskite.

CRediT authorship contribution statement

Alex Sembito: Writing – review & editing, Writing – original draft, Methodology, Investigation, Formal analysis, Data curation, Conceptualization. **Margdaline Musanga Ligavo:** Writing – review & editing, Writing – original draft. **Julius M. Mwabora:** Writing – review & editing, Supervision, Resources, Funding acquisition. **Francis W. Nyongesa:** Writing – review & editing, Supervision, Resources, Funding acquisition, Conceptualization. **Mmantsae Diale:** Writing – review & editing, Validation, Supervision, Resources, Project administration, Methodology, Funding acquisition, Conceptualization.

Declaration of competing interest

The authors declare that they have no known competing financial interests or personal relationships that could have appeared to influence the work reported in this paper.

Acknowledgements

The authors thank Regional Scholarship and Innovation Fund (RSIF) established by Partnership for Skills in Applied Sciences, Engineering and Technology (PASET) and South African Research chair (SARChI), UID 115463 for funding. Francois Conradie is also acknowledged for measurements of PL and TRPL. University of Nairobi (UoN) partnership with University of Pretoria is acknowledged for providing access to laboratories for synthesis and characterization of the films.

Appendix A. Supplementary data

Supplementary data to this article can be found online at https://doi.

org/10.1016/j.vacuum.2024.113954.

Data availability

Data will be made available on request.

References

[1] L. Gao, L.N. Quan, F.P. García de Arquer, Y. Zhao, R. Munir, A. Proppe, R. Quintero-Bermudez, C. Zou, Z. Yang, M.I. Saidaminov, O. Voznyy, S. Kinge, Z. Lu, S.O. Kelley, A. Amassian, J. Tang, E.H. Sargent, Efficient near-infrared light-emitting diodes based on quantum dots in layered perovskite, Nat. Photonics 14 (2020) 227–233, https://doi.org/10.1038/s41566-019-0577-1.

[2] J. Burschka, N. Pellet, S.-J. Moon, R. Humphry-Baker, P. Gao, M.K. Nazeeruddin, M. Grätzel, Sequential deposition as a route to high-performance perovskite-sensitized solar cells, Nature 499 (2013) 316–319, https://doi.org/10.1038/nature12340.

[3] C.C. Vidyasagar, B.M. Muñoz Flores, V.M. Jiménez Pérez, Recent advances in synthesis and properties of hybrid halide perovskites for photovoltaics, Nano-Micro Lett. 10 (2018) 68, https://doi.org/10.1007/s40820-018-0221-5.

[4] Intrinsic thermal instability of methylammonium lead trihalide perovskite - conings - 2015 - advanced energy materials - wiley online library (n.d.), https://onlinelibrary-wiley-com.uplib.idm.oclc.org/doi/full/10.1002/aenm.201500477. (Accessed 26 February 2024).

[5] J. Huang, S. Tan, P.D. Lund, H. Zhou, Impact of H2O on organic–inorganic hybrid perovskite solar cells, Energy Environ. Sci. 10 (2017) 2284–2311, https://doi.org/10.1039/C7EE01674C.

[6] Z. Cheng, J. Lin, Layered organic–inorganic hybrid perovskites: structure, optical properties, film preparation, patterning and templating engineering, CrystEngComm 12 (2010) 2646–2662, https://doi.org/10.1039/C001929A.

[7] Z. Tan, Y. Wu, H. Hong, J. Yin, J. Zhang, L. Lin, M. Wang, X. Sun, L. Sun, Y. Huang, K. Liu, Z. Liu, H. Peng, Two-dimensional (C4H9NH3)2PbBr4 perovskite crystals for high-performance photodetector, J. Am. Chem. Soc. 138 (2016) 16612–16615, https://doi.org/10.1021/jacs.6b11683.

[8] B.-B. Yu, Z. Chen, Y. Zhu, Y. Wang, B. Han, G. Chen, X. Zhang, Z. Du, Z. He, Heterogeneous 2D/3D tin-halides perovskite solar cells with certified conversion efficiency breaking 14, Adv. Mater. 33 (2021) 2102055, https://doi.org/10.1002/adma.202102055.

[9] E.S. Parrott, R.L. Milot, T. Stergiopoulos, H.J. Snaith, M.B. Johnston, L.M. Herz, Effect of structural phase transition on charge-carrier lifetimes and defects in CH3NH3SnI3 perovskite, J. Phys. Chem. Lett. 7 (2016) 1321–1326, https://doi.org/10.1021/acs.jpclett.6b00322.

[10] M. Awais, R.L. Kirsch, V. Yeddu, M.I. Saidaminov, Tin halide perovskites going forward: frost diagrams offer hints, ACS Mater. Lett. 3 (2021) 299–307, https://doi.org/10.1021/acsmaterialslett.0c00571.

[11] L. Gu, D. Li, L. Chao, H. Dong, W. Hui, T. Niu, C. Ran, Y. Xia, L. Song, Y. Chen, W. Huang, Strain engineering of metal–halide perovskites toward efficient photovoltaics: advances and perspectives, Sol. RRL 5 (2021) 2000672, https://doi.org/10.1002/solr.202000672.

[12] H. Dong, C. Ran, W. Gao, N. Sun, X. Liu, Y. Xia, Y. Chen, W. Huang, Crystallization dynamics of Sn-based perovskite thin films: toward efficient and stable photovoltaic devices, Adv. Energy Mater. 12 (2022) 2102213, https://doi.org/10.1002/aenm.202102213.

[13] J. Ávila, C. Momblona, P.P. Boix, M. Sessolo, H.J. Bolink, Vapor-deposited perovskites: the route to high-performance solar cell production? Joule 1 (2017) 431–442, https://doi.org/10.1016/j.joule.2017.07.014.

[14] J.N. Fru, N. Nombona, M. Diale, Characterization of sequential physical vapor deposited methylammonium lead tri-iodide perovskite thin films, Vacuum 182 (2020) 109727, https://doi.org/10.1016/j.vacuum.2020.109727.

[15] Y. Yu, D. Zhao, C.R. Grice, W. Meng, C. Wang, W. Liao, A.J. Cimaroli, H. Zhang, K. Zhu, Y. Yan, Thermally evaporated methylammonium tin triiodide thin films for lead-free perovskite solar cell fabrication, RSC Adv. 6 (2016) 90248–90254, https://doi.org/10.1039/C6RA19476A.

[16] M.G. La Placa, D. Guo, L. Gil-Escrig, F. Palazon, M. Sessolo, H. Bolink, Dual-source vacuum deposition of pure and mixed halide 2D perovskites: thin film characterization and processing guidelines, J. Mater. Chem. C 8 (2020), https://doi.org/10.1039/C9TC06662D.

[17] J.N. Fru, N. Nombona, M. Diale, Synthesis and characterisation of methylammonium lead tri-bromide perovskites thin films by sequential physical vapor deposition, Phys. B Condens. Matter 578 (2020) 411884, https://doi.org/10.1016/j.physb.2019.411884.

[18] D. Moghe, L. Wang, C.J. Traverse, A. Redoute, M. Sponseller, P.R. Brown, V. Bulović, R.R. Lunt, All vapor-deposited lead-free doped CsSnBr3 planar solar cells, Nano Energy 28 (2016) 469–474, https://doi.org/10.1016/j.nanoen.2016.09.009.

[19] A. Sembito, J.M. Mwabora, F.W. Nyongesa, M. Diale, The effect of guanidinium tetrafluoroborate surface passivation on the stability of 2D-PEA2SnI4 perovskite thin films prepared by sequential physical vapor deposition, Phys. B Condens. Matter 697 (2025) 416735. https://doi.org/10.1016/j.physb.2024.416735.

[20] C.R. Kagan, D.B. Mitzi, C.D. Dimitrakopoulos, Organic-inorganic hybrid materials as semiconducting channels in thin-film field-effect transistors, Science 286 (1999) 945–947, https://doi.org/10.1126/science.286.5441.945.

[21] C.G. Pope, X-ray diffraction and the Bragg equation, J. Chem. Educ. 74 (1997) 129, https://doi.org/10.1021/ed074p129.

[22] A. Ham, T.S. Kim, M. Kang, H. Cho, K. Kang, Strategies for chemical vapor deposition of two-dimensional organic-inorganic halide perovskites, iScience 24 (2021). https://www.cell.com/iscience/pdf/S2589-0042(21)01457-7.pdf. (Accessed 4 March 2024).

[23] Z.-G. Ma, Y. Shen, K. Zhang, L.-X. Cao, H. Ren, W.-S. Chen, H.-X. Wei, Y.-Q. Li, S. Kera, J.-X. Tang, Regulated crystallization with minimized degradation for pure-red lead-free perovskite light-emitting diodes, J. Mater. Chem. C 11 (2023) 9916–9924, https://doi.org/10.1039/D3TC01743E.

[24] X. Lian, J. Chen, Y. Zhang, M. Qin, J. Li, S. Tian, W. Yang, X. Lu, G. Wu, H. Chen, Highly efficient Sn/Pb binary perovskite solar cell via precursor engineering: a two-step fabrication process, Adv. Funct. Mater. 29 (2019) 1807024, https://doi.org/10.1002/adfm.201807024.

[25] R. Rotaru, M. Savin, N. Tudorachi, C. Peptu, P. Samoila, L. Sacarescu, V. Harabagiu, Ferromagnetic iron oxide–cellulose nanocomposites prepared by ultrasonication, Polym. Chem. 9 (2018) 860–868.

[26] Z. Peng, Su, W. Zheng, P. Lan, C. Luo, Z. Fan, X. Liang, High-quality perovskite CH3NH3PbI3 thin films for solar cells prepared by single-source thermal evaporation combined with solvent treatment, Materials 12 (2019) 1237, https://doi.org/10.3390/ma12081237.

[27] V.S. Vinila, J. Isac, Synthesis and structural studies of superconducting perovskite GdBa2Ca3Cu4O10. 5+ δ nanosystems, in: Des. Fabr. Charact. Multifunct. Nanomater., Elsevier, 2022, pp. 319–341. https://www.sciencedirect.com/science/article/pii/B9780128205587000224. (Accessed 14 November 2023).

[28] M.M. Abdelhamied, Y. Gao, X. Li, W. Liu, Boosting the photoluminescence of 2D organic–inorganic perovskite films by mixing with polymers, Appl. Phys. A 128 (2022) 57, https://doi.org/10.1007/s00339-021-05189-y.

[29] M.A. Islam, H. Mohafez, K. Sobayel, S.F. Wan Muhamad Hatta, A.K.M. Hasan, M. U. Khandaker, M. Akhtaruzzaman, G. Muhammad, N. Amin, Degradation of perovskite thin films and solar cells with candle soot C/Ag electrode exposed in a control ambient, Nanomaterials 11 (2021) 3463, https://doi.org/10.3390/nano11123463.

[30] M.-H. Li, H.-H. Yeh, Y.-H. Chiang, U.-S. Jeng, C.-J. Su, H.-W. Shiu, Y.-J. Hsu, N. Kosugi, T. Ohigashi, Y.-A. Chen, P.-S. Shen, P. Chen, T.-F. Guo, Highly efficient 2D/3D hybrid perovskite solar cells via low-pressure vapor-assisted solution process, Adv. Mater. 30 (2018) 1801401, https://doi.org/10.1002/adma.201801401.

[31] W.-G. Choi, C.-G. Park, Y. Kim, T. Moon, Sn perovskite solar cells via 2D/3D bilayer formation through a sequential vapor process, ACS Energy Lett. 5 (2020) 3461–3467, https://doi.org/10.1021/acsenergylett.0c01887.

[32] H. Duim, S. Adjokatse, S. Kahmann, G.H. ten Brink, M.A. Loi, The impact of stoichiometry on the photophysical properties of ruddlesden–popper perovskites, Adv. Funct. Mater. 30 (2020) 1907505, https://doi.org/10.1002/adfm.201907505.

[33] M.Y.A. Mat Yunin, N. Mohd Adenam, W.M. Khairul, A.H. Yusoff, H.K. Adli, Effect of stability of two-dimensional (2D) aminoethyl methacrylate perovskite using lead-based materials for ammonia gas sensor application, Polymers 14 (2022) 1853, https://doi.org/10.3390/polym14091853.

[34] M.A. Islam, H. Mohafez, K. Sobayel, S.F. Wan Muhamad Hatta, A.K.M. Hasan, M. U. Khandaker, Md Akhtaruzzaman, G. Muhammad, N. Amin, Degradation of perovskite thin films and solar cells with candle soot C/Ag electrode exposed in a control ambient, Nanomaterials 11 (2021) 3463, https://doi.org/10.3390/nano11123463.

[35] M. Jamal, A. Shahahmadi, P. Chelvanathan, H. Alharbi, M. Karim, M. Mohammed, N. Alharth, Y. Al-Harthi, M. Aminuzzaman, N. Asim, K. Sopian, S.K. Tiong, N. Amin, M. Akhtaruzzaman, Effects of growth temperature on the photovoltaic properties of RF sputtered undoped NiO thin films, Results Phys. 14 (2019) 102360, https://doi.org/10.1016/j.rinp.2019.102360.

[36] H. Zhang, C. Zhao, D. Li, H. Guo, F. Liao, W. Cao, X. Niu, Y. Zhao, Effects of substrate temperature on the crystallization process and properties of mixed-ion perovskite layers, J. Mater. Chem. A 7 (2019) 2804–2811, https://doi.org/10.1039/C8TA10170A.

[37] K.B. Lohmann, J.B. Patel, M.U. Rothmann, C.Q. Xia, R.D.J. Oliver, L.M. Herz, H. J. Snaith, M.B. Johnston, Control over crystal size in vapor deposited metal-halide perovskite films, ACS Energy Lett. 5 (2020) 710, https://doi.org/10.1021/acsenergylett.0c00183.

[38] Y. Ju, X. Wu, S. Huang, G. Dai, T. Song, H. Zhong, The evolution of photoluminescence properties of PEA2SnI4 upon oxygen exposure: insight into concentration effects, Adv. Funct. Mater. 32 (2022) 2108296, https://doi.org/10.1002/adfm.202108296.

[39] R. Li, C. Yi, R. Ge, W. Zou, L. Cheng, N. Wang, J. Wang, W. Huang, Room-temperature electroluminescence from two-dimensional lead halide perovskites, Appl. Phys. Lett. 109 (2016) 151101, https://doi.org/10.1063/1.4964413.

[40] D.O. Oyewole, R.K. Koech, R. Ichwani, R. Ahmed, J. Hinostroza Tamayo, S. A. Adeniji, J. Cromwell, E. Colin Ulloa, O.K. Oyewole, B. Agyei-Tuffour, L. V. Titova, N.A. Burnham, W.O. Soboyejo, Annealing effects on interdiffusion in layered FA-rich perovskite solar cells, AIP Adv. 11 (2021) 065327, https://doi.org/10.1063/5.0046205.

[41] K.-R. Yun, T.-J. Lee, S.-K. Kim, J.-H. Kim, T.-Y. Seong, Fast and highly sensitive photodetectors based on Pb-free Sn-based perovskite with additive engineering, Adv. Opt. Mater. 11 (2023) 2201974, https://doi.org/10.1002/adom.202201974.

[42] N. Ali, X. Wang, H. Wu, 16 - lower dimensional nontoxic perovskites: structures, optoelectronic properties, and applications, in: V.K. Tewary, Y. Zhang (Eds.), Model. Charact. Prod. Nanomater, second ed., Woodhead Publishing, 2023, pp. 437–466, https://doi.org/10.1016/B978-0-12-819905-3.00016-6.

[43] A.D. Dhondge, S.R. Gosavi, N.M. Gosavi, C.P. Sawant, A.M. Patil, A.R. Shelke, N. G. Deshpande, Influence of thickness on the photosensing properties of chemically

synthesized copper sulfide thin films, World J. Condens. Matter Phys. 5 (2015) 1–9, https://doi.org/10.4236/wjcmp.2015.51001.
[44] Y.-Q. Zhao, Q.-R. Ma, B. Liu, Z.-L. Yu, J. Yang, M.-Q. Cai, Layer-dependent transport and optoelectronic property in two-dimensional perovskite: (PEA) $_2$ PbI $_4$, Nanoscale 10 (2018) 8677–8688, https://doi.org/10.1039/C8NR00997J.
[45] A. Kumar, S. Singh, M.K.A. Mohammed, A. Esmail Shalan, Effect of 2D perovskite layer and multivalent defect on the performance of 3D/2D bilayered perovskite solar cells through computational simulation studies, Sol. Energy 223 (2021) 193–201, https://doi.org/10.1016/j.solener.2021.05.042.
[46] T. Yokoyama, D.H. Cao, C.C. Stoumpos, T.-B. Song, Y. Sato, S. Aramaki, M. G. Kanatzidis, Overcoming short-circuit in lead-free CH3NH3SnI3 perovskite solar cells via kinetically controlled gas–solid reaction film fabrication process, ACS Publ (2016), https://doi.org/10.1021/acs.jpclett.6b00118.
[47] M.-G. La-Placa, D. Guo, L. Gil-Escrig, F. Palazon, M. Sessolo, H.J. Bolink, Dual-source vacuum deposition of pure and mixed halide 2D perovskites: thin film characterization and processing guidelines, J. Mater. Chem. C 8 (2020) 1902–1908, https://doi.org/10.1039/C9TC06662D.
[48] C. Bi, Y. Shao, Y. Yuan, Z. Xiao, C. Wang, Y. Gao, J. Huang, Understanding the formation and evolution of interdiffusion grown organolead halide perovskite thin films by thermal annealing, J. Mater. Chem. A 2 (2014) 18508–18514, https://doi.org/10.1039/C4TA04007D.
[49] Q. Zhang, L. Chu, F. Zhou, W. Ji, G. Eda, Excitonic properties of chemically synthesized 2D organic–inorganic hybrid perovskite nanosheets, Adv. Mater. 30 (2018) 1704055, https://doi.org/10.1002/adma.201704055.
[50] O. Oyelade, O. Oyewole, Y. Olanrewaju, R. Ichwani, R. Koech, D. Oyewole, S. Adeniji, D. Sanni, J. Cromwell, R. Ahmed, K. Orisekeh, V.C. Anye, W. Soboyejo, Understanding the effects of annealing temperature on the mechanical properties of layers in FAI-rich perovskite solar cells, AIP Adv. 12 (2022) 025104, https://doi.org/10.1063/5.0078558.